

# ANALYSIS OF HESSIAN SCALING FOR LOCAL AND GLOBAL COSTS IN VARIATIONAL QUANTUM ALGORITHMS

YIHAN HUANG\* AND YANGSHUAI WANG†

**Abstract.** Barren plateaus are typically characterized by vanishing gradients, yet the feasibility of curvature-based optimization fundamentally relies on the statistical resolvability of the Hessian matrix. In this work, we quantify the entrywise resolvability of the Hessian for Variational Quantum Algorithms at random initialization. By leveraging exact second-order parameter-shift rules, we derive a structural representation that reduces the variance of Hessian entries to a finite covariance quadratic form of shifted cost evaluations. This framework reveals two distinct scaling regimes that govern the sample complexity required to resolve Hessian entries against shot noise. For global objectives, we prove that Hessian variances are exponentially suppressed, implying that the number of measurement shots must scale as  $O(e^{\alpha n})$  with the number of qubits  $n$  to maintain a constant signal-to-noise ratio. In contrast, for termwise local objectives in bounded-depth circuits, the variance decay is polynomial and explicitly controlled by the backward lightcone growth on the interaction graph, ensuring that curvature information remains statistically accessible with  $O(\text{poly}(n))$  shots. Extensive numerical experiments across varying system sizes and circuit depths demonstrate these theoretical bounds and the associated sampling costs. Our results provide a rigorous criterion for the computational tractability of second-order methods at initialization.

**Key words.** variational quantum algorithms, barren plateaus, Hessian variance, parameter-shift rule, cost function locality

**MSC codes.** 81P68, 65C40, 65K10, 68Q12

**1. Introduction.** Variational quantum algorithms (VQAs) have emerged as a dominant paradigm for the noisy intermediate-scale quantum (NISQ) era, formulating problems as stochastic optimization over parameterized quantum circuits [9, 20, 28, 19, 18, 2, 37]. However, their scalability is fundamentally constrained by the geometry of the optimization landscape. Beyond the general NP-hardness of training [6], a central obstruction is the *barren plateau* phenomenon [25, 22]: for broad classes of ansatz families, gradient variances decay exponentially with system size, rendering first-order optimization ineffective at random initialization [16, 5].

The mechanisms driving this first-order information loss are now well understood. Theoretical analyses link vanishing gradients to factors such as excessive entanglement [24], the globality of the cost operator [11], and hardware noise [35]. Geometrically, these landscapes are characterized by narrow gorges [3] or a proliferation of traps [27]. In response, a diverse array of diagnostic [21] and mitigation strategies has been developed, encompassing architectural designs [29], specialized initialization techniques [16, 26], layerwise training [32], and controls on ansatz expressibility [17].

Despite this progress, a systematic second-order theory for landscape curvature remains underdeveloped. Curvature-aware strategies, including Newton-type updates and the quantum natural gradient [33], are staples of scientific computing. However, their efficacy in the quantum regime depends entirely on the statistical accessibility of curvature information as the system scales. While prior work indicates that higher-order derivatives can also vanish [10] and empirical studies have explored specific applications [31], existing theoretical analyses largely focus on global operator norms or specific backpropagation schemes [7]. These approaches overlook the *entrywise*

\*Department of Mathematics, Faculty of Science, National University of Singapore, 10 Lower Kent Ridge Road, Singapore.

†Corresponding author. Department of Mathematics, Faculty of Science, National University of Singapore, 10 Lower Kent Ridge Road, Singapore ([yswang@nus.edu.sg](mailto:yswang@nus.edu.sg)).

*statistical resolvability* of the Hessian at random initialization, a property essential for practical optimization where estimators are constructed from finite measurement budgets. Consequently, a fundamental question arises: when first-order gradients vanish, does second-order information remain statistically accessible, and what precise scaling laws govern its variance?

In this work, we bridge this gap by quantifying the initialization scaling of Hessian-entry fluctuations. Focusing on hardware-efficient architectures with bounded-depth locality, we build our analysis upon two technical pillars: the parameter-shift rule [4, 13, 36], which provides an exact framework for derivative evaluation, and the established role of cost function locality in mitigating first-order plateaus [11, 34]. By leveraging exact second-order parameter-shift identities, we express each Hessian entry as a constant-size linear combination of shifted objective evaluations. This structural representation reduces the entrywise variance  $\text{Var}_\rho(H_{jk})$  to a finite covariance–quadratic form, allowing us to control the scaling explicitly via backward-lightcone geometry. Figure 1 schematically illustrates the resulting regimes.

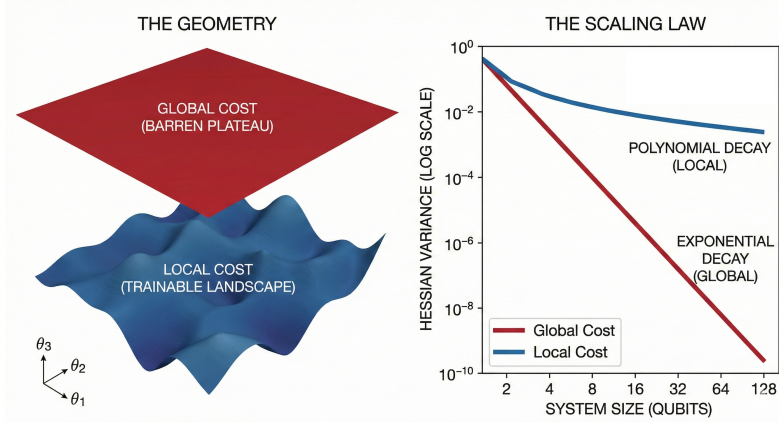


Fig. 1: **Higher-order barren plateaus: global vs. local objectives.** Schematic landscapes and expected scaling of *resolvable* Hessian-entry variance with system size: global costs can exhibit exponential suppression at initialization, while local costs retain a larger (polynomially decaying) resolvable curvature scale.

Our analysis reveals two distinct scaling regimes at random initialization. For global observables, we prove that the Hessian inherits the objective’s exponential concentration, implying that resolving curvature against shot noise requires a prohibitive  $O(e^{\alpha n})$  complexity. Conversely, for  $k$ -local objectives, we derive polynomial variance bounds explicitly governed by the ratio of the causal lightcone volume  $V_G(k + 2rL)$  to the system size  $n$ . This geometric scaling ensures that, provided the lightcone remains sub-extensive, curvature information remains statistically accessible with  $O(\text{poly}(n))$  measurements. We demonstrate this theoretical framework through numerical experiments that verify the predicted scaling laws, analyze the Hessian eigenspectra, and quantify the practical sampling complexity required for curvature estimation.

The remainder of the paper is structured as follows. In § 2, we establish the theoretical framework, including architectural assumptions and the relevant parameter-shift representations. § 3 presents our main theoretical analysis, deriving the explicit variance bounds and scaling laws that distinguish global from local objectives. These

analytical predictions are demonstrated in § 4 through extensive numerical experiments. Finally, we discuss practical implications and future directions in § 5. Detailed proofs and supplementary technical results are deferred to the appendices.

**2. Theoretical Background.** We establish the framework for VQAs needed to analyze higher-order derivatives. We define the circuit model, objective functions, and locality notions that control operator spreading, and we derive the parameter-shift identities for gradients and Hessian entries used throughout the paper. We also state the initialization assumptions and our definition of higher-order barren plateaus, which underpin the variance bounds in § 3.

**2.1. Parameterized quantum circuits.** A parameterized quantum circuit is a family of unitaries  $\{U(\boldsymbol{\theta})\}_{\boldsymbol{\theta} \in \mathbb{R}^M}$  acting on the  $n$ -qubit Hilbert space  $\mathcal{H}_n = (\mathbb{C}^2)^{\otimes n}$ , where  $M$  is the number of parameters. For each  $\boldsymbol{\theta}$ , the circuit prepares

$$(2.1) \quad |\psi(\boldsymbol{\theta})\rangle = U(\boldsymbol{\theta})|0\rangle^{\otimes n} \in \mathcal{H}_n.$$

We focus on hardware-efficient architectures of depth  $L$  obtained by alternating fixed entangling layers and parameterized rotations. Specifically, each layer  $\ell$  consists of a parameter-independent entangling unitary  $V_\ell \in U(2^n)$  followed by  $m_\ell$  parametrized gates, so that

$$(2.2) \quad U(\boldsymbol{\theta}) = \prod_{\ell=1}^L \left( V_\ell \prod_{j=1}^{m_\ell} \exp(-i\theta_{\ell,j} G_{\ell,j}) \right),$$

with products ordered in increasing  $\ell$  (as written) and  $M = \sum_{\ell=1}^L m_\ell$ . When convenient we index parameters by a single label  $a \in \{1, \dots, M\}$ , with  $a$  corresponding to a unique pair  $(\ell, j)$  in (2.2).

To enable exact constant-cost parameter-shift rules for gradients and Hessians, we assume each parametrized gate has a two-point-spectrum generator (e.g., Pauli rotations). We note that more general spectra admit generalized shift rules with a larger constant overhead.

*Assumption 2.1* (Two-point-spectrum generators). In (2.2), each generator  $G_{\ell,j}$  is Hermitian and supported on at most  $r$  qubits, where  $r$  is independent of  $n$ . Moreover,  $G_{\ell,j}$  has a two-point spectrum  $\text{spec}(G_{\ell,j}) = \{\pm\gamma\}$  for some  $\gamma > 0$ . Without loss of generality we take  $\gamma = \frac{1}{2}$ , i.e.,

$$(2.3) \quad G_{\ell,j}^2 = \frac{1}{4}I \quad \text{equivalently} \quad \text{spec}(G_{\ell,j}) = \{\pm\frac{1}{2}\}.$$

This includes Pauli rotations  $G_{\ell,j} = P_{\ell,j}/2$  with  $P_{\ell,j}$  a Pauli string supported on at most  $r$  qubits.

**2.2. Cost functions and locality.** The objective is to minimize the expectation value of a Hermitian observable  $O$  under the variational state  $|\psi(\boldsymbol{\theta})\rangle$ :

$$(2.4) \quad C(\boldsymbol{\theta}) = \langle \psi(\boldsymbol{\theta}) | O | \psi(\boldsymbol{\theta}) \rangle = \langle 0 | U^\dagger(\boldsymbol{\theta}) O U(\boldsymbol{\theta}) | 0 \rangle.$$

Locality of  $O$  controls the spatial scale on which the conjugated observable  $U^\dagger(\boldsymbol{\theta}) O U(\boldsymbol{\theta})$  can spread, and thus the dependence structure underlying the variance bounds in § 3.

**DEFINITION 2.2** (Local versus global objectives). *An observable  $O$  is  $k$ -local if it acts nontrivially on at most  $k$  qubits, i.e.,  $|\text{supp}(O)| \leq k$  for a constant  $k$  independent*

of  $n$ . More generally, an objective  $C(\boldsymbol{\theta})$  is  $k$ -local termwise if it can be written as  $C(\boldsymbol{\theta}) = \frac{1}{n} \sum_{i=1}^n \langle \psi(\boldsymbol{\theta}) | O_i | \psi(\boldsymbol{\theta}) \rangle$  with each  $O_i$  being  $k$ -local. We call an observable  $O$  (and the objective it induces via (2.4)) global if it has extensive support, i.e.,  $|\text{supp}(O)|$  grows linearly with  $n$ .

A canonical global example is

$$(2.5) \quad O_{\text{glo}} = Z^{\otimes n}, \quad C_{\text{glo}}(\boldsymbol{\theta}) = \langle \psi(\boldsymbol{\theta}) | Z^{\otimes n} | \psi(\boldsymbol{\theta}) \rangle,$$

which acts nontrivially on all qubits. In contrast, local objectives are typically constructed from bounded-support terms, e.g.,  $Z_i$  or  $Z_i Z_{i+1}$ . For normalization one often considers averaged local costs, for instance

$$(2.6) \quad C_{\text{loc}}(\boldsymbol{\theta}) = \frac{1}{n} \sum_{i=1}^n \langle \psi(\boldsymbol{\theta}) | Z_i | \psi(\boldsymbol{\theta}) \rangle,$$

which remains 1-local termwise while producing an  $O(1)$ -scaled objective.

**2.3. Parameter-shift identities.** Under Assumption 2.1, derivatives of  $C(\boldsymbol{\theta})$  admit exact two-shift parameter-shift formulas [13]. In particular,

$$(2.7) \quad \frac{\partial C}{\partial \theta_j} = \frac{1}{2} \left[ C(\boldsymbol{\theta} + \frac{\pi}{2} \mathbf{e}_j) - C(\boldsymbol{\theta} - \frac{\pi}{2} \mathbf{e}_j) \right],$$

where  $\mathbf{e}_j$  denotes the  $j$ -th canonical basis vector in  $\mathbb{R}^M$ . Applying (2.7) twice yields the Hessian entries. For  $j \neq k$ ,

$$(2.8) \quad H_{jk} = \frac{1}{4} \left[ C(\boldsymbol{\theta} + \frac{\pi}{2} \mathbf{e}_j + \frac{\pi}{2} \mathbf{e}_k) - C(\boldsymbol{\theta} + \frac{\pi}{2} \mathbf{e}_j - \frac{\pi}{2} \mathbf{e}_k) - C(\boldsymbol{\theta} - \frac{\pi}{2} \mathbf{e}_j + \frac{\pi}{2} \mathbf{e}_k) + C(\boldsymbol{\theta} - \frac{\pi}{2} \mathbf{e}_j - \frac{\pi}{2} \mathbf{e}_k) \right],$$

and for  $j = k$ ,

$$(2.9) \quad H_{jj} = \frac{1}{4} \left[ C(\boldsymbol{\theta} + \pi \mathbf{e}_j) - 2C(\boldsymbol{\theta}) + C(\boldsymbol{\theta} - \pi \mathbf{e}_j) \right].$$

For more general generator spectra, generalized parameter-shift rules still yield finite linear combinations of shifted costs [36]. We note that our results only require an  $O(1)$  number of shifts per derivative.

**2.4. Trainability metrics at random initialization.** We analyze gradient and Hessian fluctuations at random initialization. Unless otherwise stated, all expectations and variances are with respect to  $\boldsymbol{\theta} \sim \rho$ , where  $\rho$  is the product measure of i.i.d. uniforms on  $[0, 2\pi)$ . We assume one parameter per gate instance in (2.2) (i.e., no parameter tying), so that  $\boldsymbol{\theta} = \{\theta_{\ell,j}\}_{(\ell,j) \in \mathcal{I}}$  indexes all parametrized gates.

*Assumption 2.3* (Depth regime). The circuit depth  $L$  is either fixed or grows sublinearly with  $n$ ; in particular,  $rL = o(n)$  as  $n \rightarrow \infty$ , where  $r$  is the gate locality from Assumption 2.1 (each generator acts on at most  $r$  qubits).

Under Assumptions 2.1 and 2.3, and for a  $k$ -local observable  $O$  in Definition 2.2, conjugation by  $U(\boldsymbol{\theta})$  expands the support of  $O$  only within a backward lightcone of radius  $O(rL)$ . We will quantify the corresponding neighborhood growth via the graph growth function  $V_G(\cdot)$  introduced in § 3.2.

*Assumption 2.4* (Observable normalization). The observable  $O$  in (2.4) is Hermitian and satisfies  $\|O\| \leq 1$ . For termwise local objectives  $C(\boldsymbol{\theta}) = \frac{1}{n} \sum_{i=1}^n \langle \psi(\boldsymbol{\theta}) | O_i | \psi(\boldsymbol{\theta}) \rangle$ , we also assume  $\|O_i\| \leq 1$ .

This normalization ensures that asymptotic variance rates reflect circuit geometry rather than trivial rescaling. We therefore quantify trainability at initialization through variance-based resolvability metrics as follows.

**2.4.1. Variance of Hessian entries.** For any indices  $(j, k)$ , we quantify Hessian-entry fluctuations at initialization by

$$(2.10) \quad \text{Var}_\rho(H_{jk}) = \mathbb{E}_\rho[H_{jk}^2] - (\mathbb{E}_\rho[H_{jk}])^2.$$

We view  $\text{Var}_\rho(H_{jk})$  as a measure of the *statistical resolvability* of entrywise curvature under finite-budget derivative estimators.

**DEFINITION 2.5** (Higher-order barren plateau). *Let  $C(\boldsymbol{\theta})$  be the cost (2.4) with Hessian  $H(\boldsymbol{\theta})$ . We say the circuit exhibits a higher-order barren plateau at initialization (entry-wise) if there exist constants  $c, \alpha > 0$  independent of  $n$  such that*

$$(2.11) \quad \text{Var}_\rho(H_{jk}) \leq c e^{-\alpha n} \quad \text{for all } j, k \text{ and all sufficiently large } n.$$

Definition 2.5 is entrywise and does not by itself imply spectral conditioning (e.g., bounds on extremal eigenvalues or condition numbers); small typical entries can still coexist with a few directions of non-negligible curvature. Nevertheless, entrywise second-moment control is the natural notion for finite-budget shift-based estimation and yields, for instance,  $\mathbb{E}_\rho[\|H\|_2^2] \leq \mathbb{E}_\rho[\|H\|_F^2] = \sum_{j,k} \mathbb{E}_\rho[H_{jk}^2]$ .

The following lemma reduces Hessian-entry variance to a covariance quadratic form over finitely many shifted objective evaluations, which is the starting point for our global/local scaling analysis. The proof is given in Appendix A.1.1.

**LEMMA 2.6** (Parameter-shift covariance representation). *Under Assumption 2.1, the diagonal Hessian entry admits the second-order parameter-shift representation*

$$(2.12) \quad H_{jj} = \frac{1}{4} \left( C(\boldsymbol{\theta} + \pi \mathbf{e}_j) - 2C(\boldsymbol{\theta}) + C(\boldsymbol{\theta} - \pi \mathbf{e}_j) \right).$$

Define  $C_+ := C(\boldsymbol{\theta} + \pi \mathbf{e}_j)$ ,  $C_0 := C(\boldsymbol{\theta})$ , and  $C_- := C(\boldsymbol{\theta} - \pi \mathbf{e}_j)$ , and let  $\Sigma \in \mathbb{R}^{3 \times 3}$  be the covariance matrix with entries  $\Sigma_{\alpha\beta} := \text{Cov}_\rho(C_\alpha, C_\beta)$  for  $\alpha, \beta \in \{+, 0, -\}$ . Then

$$(2.13) \quad \text{Var}_\rho(H_{jj}) = a^\top \Sigma a, \quad a := \frac{1}{4}(1, -2, 1)^\top,$$

and equivalently  $\text{Var}_\rho(H_{jj})$  can be written as an explicit linear combination of variances and covariances among  $\{C_+, C_0, C_-\}$ . An analogous covariance-quadratic representation holds for off-diagonal entries  $H_{jk}$  using (2.8) (see Appendix A.1.2).

Lemma 2.6 extends to any differentiation scheme that represents  $H_{jk}$  as a finite linear combination of shifted costs, provided the number of shifted evaluations is  $O(1)$ , with constants determined by the shift coefficients.

**3. Asymptotic Variance Analysis.** This section analyzes the asymptotic scaling of Hessian-entry variances. We first reduce  $\text{Var}_\rho(H_{jk})$  to a finite covariance-quadratic form over shifted cost evaluations, and then bound the resulting covariances using locality and lightcone structure for termwise local objectives, or a second-moment concentration condition for global objectives.

**3.1. Variance representation via parameter shifts.** Let  $C(\boldsymbol{\theta})$  be the cost (2.4) and let  $H_{jk}$  denote the Hessian entries given by (2.8)–(2.9). By Lemma 2.6, each  $H_{jk}$  is a fixed linear combination of finitely many shifted costs, hence  $\text{Var}_\rho(H_{jk})$  reduces to a finite covariance–quadratic form.

For each  $(j, k)$  there exist a finite shift set  $\mathcal{S}_{jk} \subset \mathbb{R}^M$  and coefficients  $\{a_s\}_{s \in \mathcal{S}_{jk}}$ , depending only on whether  $j = k$  or  $j \neq k$ , such that

(3.1)

$$\text{Var}_\rho(H_{jk}) = \text{Var}_\rho \left( \sum_{s \in \mathcal{S}_{jk}} a_s C(\boldsymbol{\theta} \oplus s) \right) = \sum_{s, s' \in \mathcal{S}_{jk}} a_s a_{s'} \text{Cov}_\rho(C(\boldsymbol{\theta} \oplus s), C(\boldsymbol{\theta} \oplus s')),$$

where  $\oplus$  denotes componentwise addition modulo  $2\pi$ . For the two-shift rules (2.8)–(2.9) one has  $|\mathcal{S}_{jk}| \leq 4$  for all  $j, k$ , and the coefficients  $\{a_s\}$  are  $O(1)$  constants independent of  $n$ . Accordingly, all constants in the bounds below may depend on the chosen shift rule but not on  $n$ . Eq. (3.1) will serve as the starting point for the variance bounds derived below.

**3.2. Main result.** This subsection derives explicit scaling bounds from (3.1) by bounding the covariances of the shifted costs. We begin with the global case and then turn to termwise  $k$ -local averaged objectives.

*Assumption 3.1* (Second-moment concentration for global objectives). Let  $O$  be Hermitian with  $\|O\| \leq 1$  and define the cost  $C(\boldsymbol{\theta})$  by (2.4). Assume there exist constants  $c_g(r, L) > 0$  and  $\alpha(r, L) > 0$ , independent of  $n$ , such that

$$(3.2) \quad \text{Var}_\rho[C(\boldsymbol{\theta})] \leq c_g(r, L) e^{-\alpha(r, L)n}.$$

Assumption 3.1 concerns second-moment concentration of the objective value at random initialization. The following analysis shows that such concentration is stable under constant-size finite-shift operators; consequently, Hessian entries computed via parameter-shift rules inherit the same exponential rate, up to constants determined by the shift coefficients (Lemma 3.2). This can be justified in two ways. (i) If the induced state ensemble forms an approximate projective 2-design, then concentration follows; Appendix B.2 proves  $\text{Var}_\rho[C(\boldsymbol{\theta})] \leq 1/(2^n + 1)$  for  $\|O\| \leq 1$  (cf. Proposition B.2). (ii) For modest-depth ansatze without such guarantees, (3.2) is directly testable via Monte Carlo estimates of  $\text{Var}_\rho[C(\boldsymbol{\theta})]$ ; by shift-invariance of  $\rho$ , the same estimate applies uniformly over the finite shift sets used in parameter-shift rules. We numerically verify this assumption in § 4.2 and give more discussion in Appendix B.2.

The next lemma records shift-uniformity and finite-shift stability of second-moment concentration, which will be used for global objectives.  $\blacksquare$

**LEMMA 3.2** (Uniform shift concentration and finite-shift transference). *Let  $\rho$  be shift-invariant on the torus, i.e.,  $\theta \sim \rho \Rightarrow \theta \oplus s \sim \rho$  for all shifts  $s \in \mathbb{R}^M$ . Fix a finite shift set  $S \subset \mathbb{R}^M$  and coefficients  $\{a_s\}_{s \in S} \subset \mathbb{R}$ , and define  $X_s := C(\theta \oplus s)$ . If  $\text{Var}_\rho[C(\theta)] \leq v_n$ , then the same bound holds uniformly over shifts,*

$$\text{Var}_\rho[X_s] = \text{Var}_\rho[C(\theta \oplus s)] = \text{Var}_\rho[C(\theta)] \leq v_n \quad \text{for all } s \in S,$$

and moreover,

$$\text{Var}_\rho \left( \sum_{s \in S} a_s C(\theta \oplus s) \right) \leq \left( \sum_{s \in S} |a_s| \right)^2 v_n.$$

*Proof.* Shift-invariance implies  $\theta$  and  $\theta \oplus s$  have the same distribution under  $\rho$ , hence  $\text{Var}_\rho[C(\theta \oplus s)] = \text{Var}_\rho[C(\theta)]$  for all  $s \in S$ . For the linear combination, by

bilinearity,

$$\text{Var} \left( \sum_{s \in S} a_s X_s \right) = \sum_{s, s' \in S} a_s a_{s'} \text{Cov}(X_s, X_{s'}).$$

By Cauchy–Schwarz,  $|\text{Cov}(X_s, X_{s'})| \leq \sqrt{\text{Var}(X_s) \text{Var}(X_{s'})} \leq v_n$ , where the last inequality uses the uniform variance bound from the first part. Therefore,

$$\text{Var} \left( \sum_{s \in S} a_s X_s \right) \leq v_n \sum_{s, s' \in S} |a_s| |a_{s'}| = v_n \left( \sum_{s \in S} |a_s| \right)^2. \quad \square$$

To make the locality bound explicit, we quantify how many local terms can have overlapping backward lightcones, which controls the maximum degree of the associated dependency graph. Let  $G$  be the interaction graph of the architecture and denote by  $B_G(v, m)$  the ball of radius  $m$  centered at  $v$ . Define the growth function

$$(3.3) \quad V_G(m) := \max_{v \in V(G)} |B_G(v, m)|.$$

For bounded-degree graphs,  $V_G(m)$  is finite for each fixed  $m$ ; for  $D$ -dimensional lattices one has  $V_G(m) = \mathcal{O}(m^D)$ .

**THEOREM 3.3** (Asymptotic scaling of Hessian-entry variance). *Under Assumptions 2.1, 2.3, and 2.4, the Hessian-entry variances satisfy, for all  $j, k \in \{1, \dots, M\}$ :*

(i) *Global objectives. If  $|\text{supp}(O)|$  grows linearly with  $n$  and Assumption 3.1 holds, then there exist constants  $\tilde{c}(r, L) > 0$  and  $\tilde{\alpha}(r, L) > 0$  such that*

$$(3.4) \quad \text{Var}_\rho(H_{jk}) \leq \tilde{c}(r, L) \exp(-\tilde{\alpha}(r, L)n).$$

(ii) *Local objectives. Suppose the cost is of the form*

$$C_{\text{loc}}(\boldsymbol{\theta}) = \frac{1}{n} \sum_{v=1}^n \langle \psi(\boldsymbol{\theta}) | O_v | \psi(\boldsymbol{\theta}) \rangle, \quad \|O_v\| \leq 1,$$

*where each  $O_v$  is supported on at most  $k$  qubits with  $k$  independent of  $n$ . Then there exists  $c_{\text{loc}}(k, r, L) > 0$  such that*

$$(3.5) \quad \text{Var}_\rho(H_{jk}) \leq c_{\text{loc}}(k, r, L) \frac{V_G(k + 2rL)}{n}.$$

*In particular, if  $V_G(m) = \mathcal{O}(m^D)$  for some fixed  $D$ , then*

$$(3.6) \quad \text{Var}_\rho(H_{jk}) \leq c_{\text{loc}}(k, r, L) \frac{(k + 2rL)^D}{n}.$$

*Proof sketch.* By the parameter-shift representation, each Hessian entry  $H_{jk}$  is a fixed  $O(1)$ -term linear combination of shifted costs  $C(\boldsymbol{\theta} \oplus s)$ , hence  $\text{Var}_\rho(H_{jk})$  reduces to a finite covariance–quadratic form over a constant-size shift set.

For global objectives, Lemma 3.2 transfers the assumed second-moment concentration of  $C(\boldsymbol{\theta})$  uniformly over the finite shifts and preserves the exponential rate under any  $O(1)$ -shift finite-difference operator, yielding (3.4).

For local objectives, bounded lightcone growth implies that local contributions with sufficiently separated supports are independent; a dependency-graph argument then gives  $\text{Var}_\rho(C(\boldsymbol{\theta} \oplus s)) = \mathcal{O}(V_G(k + 2rL)/n)$  uniformly in  $s$ . Plugging this bound into the covariance representation yields (3.5). Details are deferred to Appendix A.3.  $\square$

*Remark 3.4.* The local bound in Theorem 3.3 depends on depth only through the lightcone growth factor  $V_G(k + 2rL)$ . Hence a sufficient condition for decay with system size is that the relevant backward lightcone remains *subextensive*,  $V_G(k + 2rL) = o(n)$ . For bounded-degree  $D$ -dimensional lattices,  $V_G(s) = O(s^D)$  up to the graph diameter and then reaches system size. Therefore the bound remains vanishing provided  $k + 2rL = o(n^{1/D})$  (equivalently,  $L = o(n^{1/D})$  up to constants), whereas once  $k + 2rL$  reaches the linear system size the lightcone becomes extensive and the locality-based suppression may no longer decay with  $n$ . On small-diameter graphs (e.g., complete graphs),  $V_G$  can saturate rapidly, so this locality protection can disappear at very shallow depth. For example, in 1D chains this permits  $L = o(n)$ , while in 2D grids it requires  $L = o(\sqrt{n})$ .

*Remark 3.5.* The estimate (3.5) is an upper bound obtained via a generic dependency-graph argument and is not expected to be exponent-tight in typical instances. The key of Theorem 3.3 is the polynomial-versus-exponential resolvability dichotomy and its dependence on lightcone growth, rather than the optimal polynomial exponent.  $\blacksquare$

Theorem 3.3 establishes a sharp dichotomy at initialization: termwise local averaging with sub-extensive lightcone growth leads to polynomially decaying variance, whereas global objectives satisfying Assumption 3.1 exhibit exponential decay. These results explicitly characterize the statistical resolvability of individual Hessian entries.

**3.3. From entrywise variance to matrix-scale bounds and sample complexity.** While the entrywise bounds above quantify the typical fluctuation scale, the practical utility of curvature information depends on the measurement budget required to separate these fluctuations from statistical noise, and on how they aggregate into matrix-level properties. Throughout this subsection,  $\mathbb{E}_\rho[\cdot]$  and  $\text{Var}_\rho(\cdot)$  denote expectation and variance with respect to initialization  $\theta \sim \rho$ . When finite-shot estimation is involved, we write  $\mathbb{E}_{\text{sh}}[\cdot | \theta]$  and  $\text{Var}_{\text{sh}}(\cdot | \theta)$  for expectation and variance over measurement noise (shots), conditional on a fixed parameter value  $\theta$ .

We first record the standard implication of entrywise second-moment control for matrix norms. The proof is included for completeness in Appendix B.3.

LEMMA 3.6. *For a random matrix  $H \in \mathbb{R}^{M \times M}$  with finite second moments,*

$$\mathbb{E}\|H\|_F^2 = \sum_{j,k=1}^M \left( \text{Var}(H_{jk}) + (\mathbb{E}[H_{jk}])^2 \right), \quad \mathbb{E}\|H\|_2^2 \leq \mathbb{E}\|H\|_F^2, \quad \mathbb{E}\|H\|_2 \leq \sqrt{\mathbb{E}\|H\|_F^2}.$$

Consequently, if  $\text{Var}(H_{jk}) \leq v_n$  and  $|\mathbb{E}H_{jk}| \leq \mu_n$  for all  $j, k$ , then

$$\mathbb{E}\|H\|_F^2 \leq M^2(v_n + \mu_n^2), \quad \mathbb{E}\|H\|_2^2 \leq M^2(v_n + \mu_n^2), \quad \mathbb{E}\|H\|_2 \leq M\sqrt{v_n + \mu_n^2}.$$

Lemma 3.6 converts the entrywise statistics into matrix-scale magnitude bounds. While these bounds do not analytically constrain the spectrum (which we examine numerically in Section 4.3), they rigorously establish the vanishing scale of the operator. Applying this tool to the scalings established in Theorem 3.3 yields the following two corollaries. Corollary 3.7 bounds the typical Hessian magnitude, while Corollary 3.8 incorporates finite-shot noise to quantify the sampling cost.

COROLLARY 3.7. *Under the conditions of Theorem 3.3. Suppose further that there exists a constant  $c > 0$ , independent of  $n$ , such that  $|\mathbb{E}_\rho[H_{jk}]|^2 \leq c \text{Var}_\rho(H_{jk})$  for all  $j, k$ . Let  $v_n$  denote the entrywise variance bound from Theorem 3.3. Then*

$$\mathbb{E}_\rho\|H\|_2^2 \leq \mathbb{E}_\rho\|H\|_F^2 \lesssim M^2 v_n, \quad \mathbb{E}_\rho\|H\|_2 \lesssim M\sqrt{v_n},$$

**Algorithm 3.1** Finite-complexity estimation of a Hessian entry via parameter-shift

---

**Input:** Ansatz  $U(\boldsymbol{\theta})$ , objective  $C(\boldsymbol{\theta})$ , indices  $(j, k)$ , shots  $N$   
**Output:** Unbiased estimate  $\hat{H}_{jk}$  of the Hessian entry  $H_{jk}$

- 1:  $\hat{H}_{jk} \leftarrow 0$
- 2: **for all**  $s \in \mathcal{S}_{jk}$  **do**  $\triangleright$  Loop over shift set  $\mathcal{S}_{jk}$  with coeff.  $a_s$  (cf. § 2.3)
- 3:   Prepare  $|\psi(\boldsymbol{\theta} \oplus s)\rangle$  and measure observable  $O$  with  $N$  shots
- 4:    $\hat{C}(\boldsymbol{\theta} \oplus s) \leftarrow$  sample mean of the measurement outcomes
- 5:    $\hat{H}_{jk} \leftarrow \hat{H}_{jk} + a_s \hat{C}(\boldsymbol{\theta} \oplus s)$   $\triangleright$  Linear combination preserves unbiasedness
- 6: **end for**
- 7: **return**  $\hat{H}_{jk}$

---

with constants depending only on  $c$ .

While Corollary 3.7 bounds the intrinsic curvature scale, the practical bottleneck in VQAs is the *signal-to-noise ratio* under finite sampling. If the entrywise fluctuations  $\sqrt{\text{Var}_\rho(H_{jk})}$  are small, resolving them against shot noise becomes computationally prohibitive. The following result quantifies this sampling cost.

**COROLLARY 3.8** (Sample complexity). *Let  $\hat{H}_{jk}(\boldsymbol{\theta})$  be the estimator computed via Algorithm 3.1 using  $N$  independent shots per circuit evaluation. Since the parameter-shift rule is a fixed linear combination, the estimator variance satisfies*

$$(3.7) \quad \text{Var}_{\text{sh}}\left(\hat{H}_{jk}(\boldsymbol{\theta}) \mid \boldsymbol{\theta}\right) \leq \frac{c_S \sigma^2}{N},$$

where  $\sigma^2 \leq 1$  is the single-shot variance bound (given  $\|O\| \leq 1$ ) and  $c_S = \sum_{s \in \mathcal{S}_{jk}} a_s^2$  is a constant determined by the shift rule. Consequently, ensuring a root-mean-square estimation error of  $\varepsilon$  requires a shot complexity  $N \gtrsim c_S \sigma^2 / \varepsilon^2$ .

Theorem 3.3 and Corollary 3.8 reveal a sharp dichotomy in the computational cost of resolving Hessian entries. Targeting an  $O(1)$  signal-to-noise ratio requires the shot complexity  $N$  to scale inversely with variance. For global objectives, exponential variance suppression dictates  $N \gtrsim \exp(2\tilde{\alpha}(r, L)n)$ , rendering optimization intractable. In contrast, for termwise local objectives, polynomial decay ensures a feasible scaling  $N \gtrsim n/V_G(k + 2rL)$ , preserving statistical accessibility for sub-extensive lightcones.

Algorithm 3.1 summarizes the finite-shift procedure underlying this analysis, which serves as the basis for the numerical experiments presented in § 4.

**4. Numerical Experiments.** This section corroborates the variance-scaling predictions of § 3 and examines their practical implications under finite evaluation complexity. After describing the simulation setting and the estimators used for gradient and Hessian statistics, we report: (i) system-size and depth scaling of representative Hessian-entry variances; (ii) complementary spectral diagnostics of  $H(\boldsymbol{\theta})$  at initialization; (iii) budget-limited optimization experiments with matched oracle calls; and (iv) an additional VQE benchmark for a  $k$ -local Hamiltonian, together with quantitative spectral summary metrics linking locality to resolvable curvature.

**4.1. Experimental setup.** All simulations were performed in **Python** using **PennyLane** [4] with an exact statevector backend, so the reported statistics isolate intrinsic landscape fluctuations. We instantiate (2.2) as a layered hardware-efficient ansatz: in each layer  $\ell$ ,  $V_\ell$  is a fixed nearest-neighbor brickwork CNOT pattern and

the parametrized gates are single-qubit  $R_y$  rotations,

$$\exp(-i\theta_{\ell,j}G_{\ell,j}) = R_y(\theta_{\ell,j}), \quad G_{\ell,j} = \frac{1}{2}Y_{q(\ell,j)},$$

where  $q(\ell, j)$  maps the gate index  $j \in \{1, \dots, m_\ell\}$  to a qubit wire. Here  $m_\ell = n$  and the total number of parameters is  $M = \sum_{\ell=1}^L m_\ell = nL$ . Parameters are initialized i.i.d. as  $\theta_{\ell,j} \sim \text{U}(-\pi, \pi)$ , which is equivalent to  $\text{U}(0, 2\pi)$  up to a global shift.

We consider two objectives of different locality,

$$(4.1) \quad C_{\text{global}}(\boldsymbol{\theta}) = \langle \psi(\boldsymbol{\theta}) | Z^{\otimes n} | \psi(\boldsymbol{\theta}) \rangle, \quad C_{\text{local}}(\boldsymbol{\theta}) = \frac{1}{n} \sum_{j=1}^n \langle \psi(\boldsymbol{\theta}) | Z_j | \psi(\boldsymbol{\theta}) \rangle.$$

For each sampled initialization  $\boldsymbol{\theta}$  we evaluate gradients and Hessian entries via the parameter-shift identities (2.7)–(2.9) on the statevector backend. Unless otherwise stated, the scaling experiments use  $n \in \{2, \dots, 16\}$ ,  $L \in \{1, \dots, 12\}$ , and  $N_s = 200$  i.i.d. initializations per configuration  $(n, L)$ ; variances are computed as empirical second central moments over this ensemble.

We estimate variances by the sample variance  $\widehat{\text{Var}}$  computed over  $N_s$  i.i.d. random initializations. Exponential scalings in  $n$  are obtained by least-squares fits of  $\log \widehat{\text{Var}}$  against  $n$  (i.e.,  $\log \widehat{\text{Var}}(n) \approx a - \alpha n$ ), and polynomial scalings by least-squares fits of  $\log \widehat{\text{Var}}$  against  $\log n$  (i.e.,  $\log \widehat{\text{Var}}(n) \approx b - p \log n$ ). 95%-percentile confidence intervals for  $\widehat{\text{Var}}$  are computed by a nonparametric bootstrap with 500 replicates.

**4.2. Scaling of Hessian variance.** We first validate the system-size and depth scaling predicted by Theorem 3.3.

**4.2.1. Dependence on system size.** We examine how representative Hessian-entry variances at random initialization scale with the number of qubits  $n$ .

As a preliminary check for the global case (cf. Assumption 3.1), we estimate the objective fluctuation  $\text{Var}_\rho[C_{\text{global}}(\boldsymbol{\theta})]$  from the same initialization ensembles. Over  $n \in \{2, \dots, 16\}$  the data are well described by an exponential fit, yielding  $\text{Var}_\rho[C_{\text{global}}(\boldsymbol{\theta})] \approx \exp(-0.61 n)$ , which numerically verifies the assumption.

Figure 2 then reports empirical variances of a diagonal and an off-diagonal entry,  $\text{Var}_\rho(H_{jj})$  and  $\text{Var}_\rho(H_{jk})$ , as functions of  $n$ , for both the global and local objectives. Unless otherwise stated, results are shown for  $(j, k) = (1, 2)$ ; other index choices exhibit the same scaling up to constant prefactors.

For  $C_{\text{global}}$  (red markers), both diagonal and off-diagonal entries exhibit clear exponential decay with  $n$ . Least-squares fits of  $\log \text{Var}_\rho(H_{jj})$  and  $\log \text{Var}_\rho(H_{jk})$  versus  $n$  over  $n$  yield

$$\text{Var}_\rho(H_{jj}) \approx \exp(-0.57 n), \quad \text{Var}_\rho(H_{jk}) \approx \exp(-0.64 n),$$

consistent with Theorem 3.3 under Assumption 3.1. Via Corollary 3.8, this implies that the target resolution required to track typical entrywise curvature becomes exponentially small as  $n$  grows.  $\blacksquare$

For  $C_{\text{local}}$  (blue markers), the scaling is qualitatively different. Fitting  $\log \text{Var}_\rho(H_{jj})$  and  $\log \text{Var}_\rho(H_{jk})$  against  $\log n$  yields power-law behavior over the tested range,

$$\text{Var}_\rho(H_{jj}) \approx n^{-1.96}, \quad \text{Var}_\rho(H_{jk}) \approx n^{-2.05},$$

indicating polynomial suppression consistent with the locality-controlled regime of Theorem 3.3. We emphasize that (3.5) is an upper bound; the observed exponents should be interpreted as instance-dependent rather than universal.

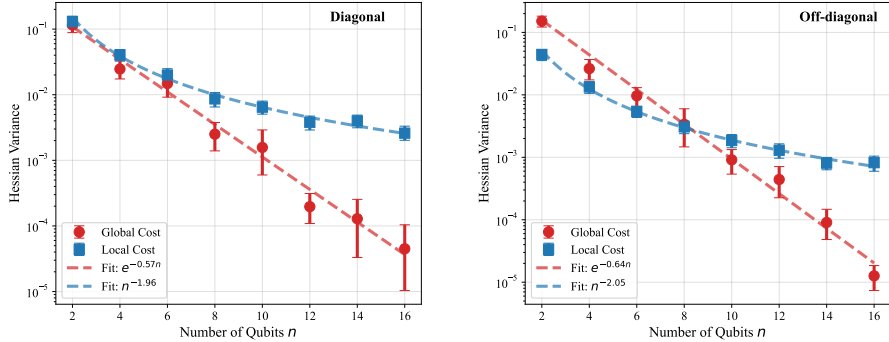


Fig. 2: **Hessian-entry variance vs. system size.**  $\text{Var}[H_{jj}]$  (left) and  $\text{Var}[H_{jk}]$  (right) versus  $n$  for  $C_{\text{global}}$  (red) and  $C_{\text{local}}$  (blue); dashed lines show exponential/power-law fits. Error bars: 95% CIs over  $N_s = 200$  initializations.

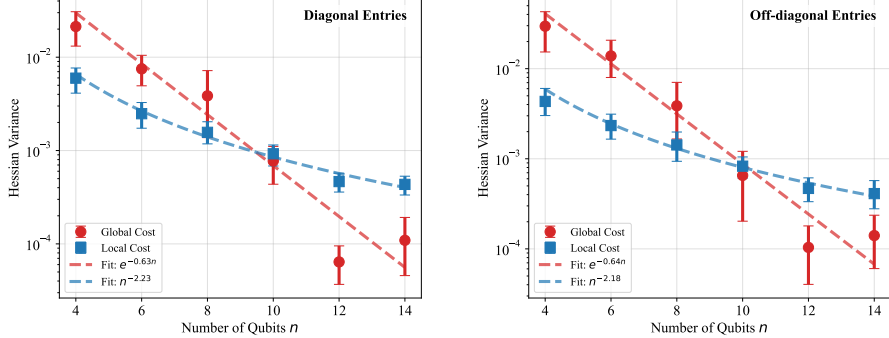


Fig. 3: **Hessian-entry variance vs. system size in a VQE task (TFIM).** Comparison of the variances of diagonal (left) and off-diagonal (right) Hessian entries between the VQE local cost (blue squares) and the global parity cost (red circles). The dashed lines represent linear regression fits.

**4.2.2. VQE with Transverse Field Ising Model.** To validate our theoretical findings in a realistic variational quantum eigensolver (VQE) setting [20], we replace the toy objective with the Hamiltonian of the 1D Transverse Field Ising Model (TFIM) [30] under periodic boundary conditions:

$$(4.2) \quad H_{\text{TFIM}} = -J \sum_{i=1}^n Z_i Z_{i+1} - h \sum_{i=1}^n X_i,$$

where we set  $J = h = 1.0$  (the critical point). The local cost function is defined as the term-wise averaged energy density  $C_{\text{local}} = \langle H_{\text{TFIM}} \rangle / (2n)$ . We compare this against a global parity observable  $O = \bigotimes_{i=1}^n Z_i$ . The variances of the Hessian entries are computed over 150 random initializations for system sizes  $n \in [4, 14]$ .

The results are presented in Fig. 3. The difference in scaling behavior is distinct: the global cost variance decays exponentially ( $\text{Var} \propto e^{-0.63n}$ ), rapidly hit-

ting the precision floor, whereas the local VQE cost follows a clear power-law decay ( $\text{Var} \propto n^{-2.2}$ ), verifying that the polynomial scaling guarantee of Theorem 3.3 holds for physical Hamiltonians with non-commuting terms. Consistent behavior is observed for both representative diagonal and off-diagonal Hessian entries.

**4.2.3. Dependence on depth.** We next examine how Hessian-entry fluctuations depend on circuit depth  $L$ , which provides a numerical view of how increasing operator spreading affects second-order resolvability. Figure 4 reports empirical variances of representative diagonal and off-diagonal entries at fixed system size  $n = 16$  over the depth range  $L \in \{1, \dots, 12\}$ .

For  $C_{\text{global}}$  (red markers), both  $\text{Var}_\rho(H_{jj})$  and  $\text{Var}_\rho(H_{jk})$  are already on the order of  $10^{-5}$  by depth  $L = 2$  and exhibit only weak additional dependence on  $L$  over the explored range. This behavior is consistent with the global-support regime: backward lightcones overlap extensively even at shallow depth, so cancellations can suppress entrywise curvature fluctuations early, leaving little variation to resolve at the scale of our reported statistics.

For  $C_{\text{local}}$  (blue markers), the variances are substantially larger at small depth (exceeding the global values by more than two orders of magnitude at  $L = 2$  in our experiments) and decrease monotonically as  $L$  increases. This trend aligns with the operator-spreading picture in § 3: as  $L$  grows, the backward lightcone of each local term expands, increasing the number of contributing components and enhancing cancellations, which reduces the typical curvature scale. Notably, across the entire depth range in Fig. 4, the local objective retains markedly larger Hessian-entry fluctuations than the global objective, supporting the conclusion that locality delays curvature concentration at moderate depths. This depth dependence is consistent with the growth factor  $V_G(k + 2rL)$  appearing in (3.5).

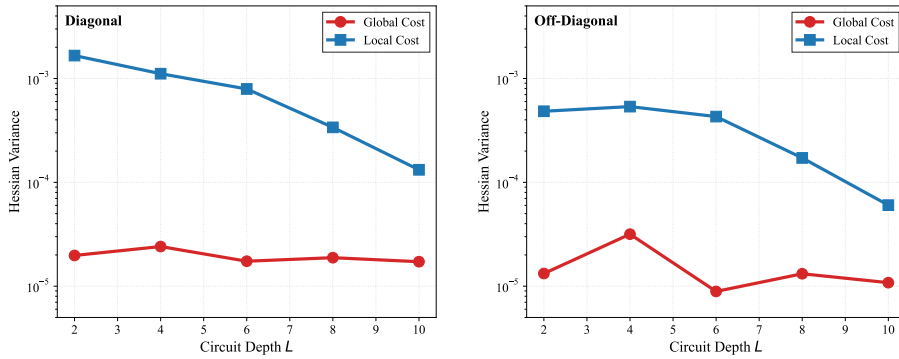


Fig. 4: **Depth dependence of Hessian-entry variance.**  $\text{Var}_\rho(H_{jj})$  (left) and  $\text{Var}_\rho(H_{jk})$  (right) versus depth  $L$  at  $n = 16$  for  $C_{\text{global}}$  (red) and  $C_{\text{local}}$  (blue).

**4.2.4. Robustness against measurement shot noise.** Fig. 5(a) quantifies how finite-shot noise affects Hessian-entry estimation under random initialization. For a fixed index pair  $(j, k)$ , we form the finite-shift estimator  $\widehat{H}_{jk}(\boldsymbol{\theta}) = \sum_{s \in \mathcal{S}_{jk}} a_s \widehat{C}(\boldsymbol{\theta} \oplus s)$ , where  $\widehat{C}(\cdot)$  is obtained from  $N$  shots per circuit evaluation. As discussed in Corollary 3.8, the estimator variability decomposes into an initialization-induced term and a shot-noise term. Concretely, when averaging over both initialization  $\boldsymbol{\theta} \sim \rho$  and measurement noise, the total variance obeys the two-term scaling  $\text{Var}_{\rho, \text{sh}}(\widehat{H}_{jk}) \approx a +$

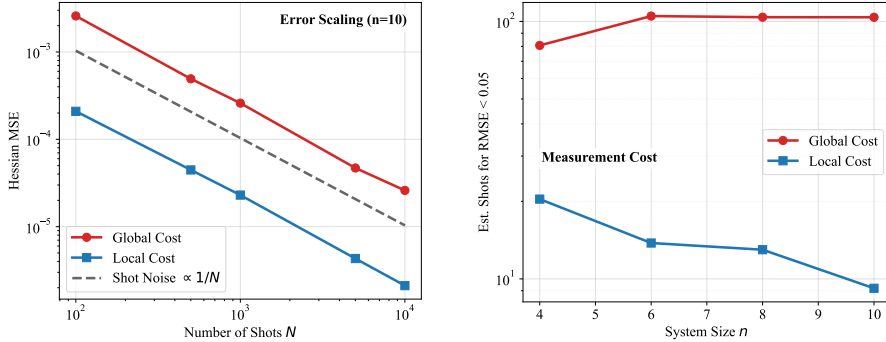


Fig. 5: **Impact of finite measurement on Hessian estimation.** Same Hessian entry and initialization protocol under a global objective and a termwise local averaged objective. (Left) Total estimator variance  $\text{Var}_{\rho,\text{sh}}(\hat{H}_{jk})$  versus shots  $N$ . (Right) Empirical shot complexity  $N(\varepsilon)$  required to reach  $\sqrt{\text{Var}_{\rho,\text{sh}}(\hat{H}_{jk})} \leq \varepsilon$  versus  $n$ .

$\frac{b}{N}$ , where  $a$  captures the intrinsic initialization-scale fluctuations of the corresponding finite-shift Hessian entry (i.e.,  $\text{Var}_{\rho}(H_{jk})$ , up to shift-rule constants), and  $b/N$  arises from finite-shot sampling.

In Fig. 5(a), the measured curves are well fit by this model across the tested shot range. The separation of a constant term and a  $1/N$  term matches the variance decomposition in Corollary 3.8. Comparing objectives, the fitted parameters reflect the distinct  $n$ -scalings predicted by Theorem 3.3: the global objective exhibits rapidly shrinking intrinsic fluctuations with  $n$  but correspondingly stringent resolution demands, whereas the termwise local averaged objective follows a polynomial regime.

To summarize the practical implications, Fig. 5(b) reports an empirical shot requirement  $N(\varepsilon)$  for a prescribed tolerance  $\varepsilon$ , defined as the smallest  $N$  such that the fitted model satisfies  $\sqrt{\text{Var}_{\rho,\text{sh}}(\hat{H}_{jk})} \leq \varepsilon$ . The resulting curves show that achieving a fixed absolute tolerance becomes rapidly more expensive with  $n$  for the global objective, while the termwise local averaged objective remains substantially less demanding, consistent with the different  $n$ -scalings of  $\text{Var}_{\rho}(H_{jk})$  in Theorem 3.3.

**4.3. Spectral structure.** While our theory controls entrywise curvature fluctuations, curvature-aware procedures also depend on how curvature is distributed across parameter-space directions. We therefore report complementary spectral diagnostics based on the empirical eigenvalue distribution of the Hessian at random initialization. These results are presented as numerical diagnostics and are not interpreted as conditioning guarantees.

*Empirical eigenspectrum.* Fig. 6 shows histogram estimates (log-density scale) of Hessian eigenvalues for global and termwise local averaged objectives at depth  $L = 4$  and increasing system size. As  $n$  grows, the spectrum associated with the global objective becomes increasingly concentrated near the origin, whereas the spectrum for the local objective remains comparatively broader over the same range. This qualitative contrast mirrors the entrywise variance behavior: global objectives exhibit a rapidly shrinking initialization-scale curvature distribution, while locality delays

such concentration for termwise averaged costs.

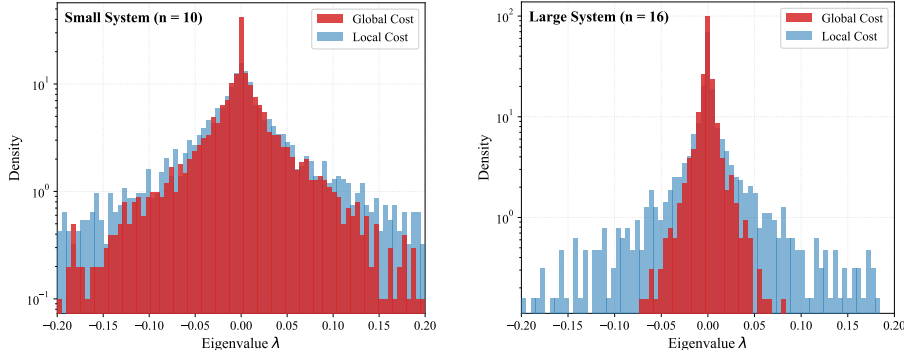


Fig. 6: **Empirical Hessian eigenspectra at depth  $L = 4$ .** Histogram estimates (log-density scale) of Hessian eigenvalues for  $C_{\text{global}}$  (red) and  $C_{\text{local}}$  (blue) at  $n = 10$  (left) and  $n = 16$  (right).

*Scalar spectral summaries.* To complement the histograms, we summarize the spectrum using two scalar metrics. The first is the root-mean-square (RMS) eigenvalue  $\lambda_{\text{RMS}} := \sqrt{\frac{1}{M} \sum_{i=1}^M \lambda_i^2}$ , which captures an overall curvature magnitude scale. The second is a thresholded near-zero eigenvalue fraction, defined for a prescribed numerical tolerance  $\varepsilon > 0$  as  $\text{Deg}_\varepsilon := \frac{1}{M} \#\{i : |\lambda_i| < \varepsilon\}$ . In Fig. 7 we report  $\text{Deg}_\varepsilon$  with  $\varepsilon = 10^{-4}$ . We emphasize that  $\text{Deg}_\varepsilon$  is resolution-dependent and should not be interpreted as a definitive statement about exact rank deficiency.

Fig. 7 (Left) shows that  $\lambda_{\text{RMS}}$  decreases with  $n$  for both objectives, consistent with an overall contraction of typical curvature magnitudes at initialization. Fig. 7 (Right) shows that, at the same numerical tolerance, the global objective exhibits a substantially larger near-zero fraction than the local averaged objective. Interpreted at fixed resolution, this indicates more directions that appear numerically flat at initialization for the global objective than for the termwise averaged local objective.

Taken together with the entrywise variance results in § 4, these spectral diagnostics provide geometric context for the observed variance scalings.

**4.4. Budget-limited manifestations.** The variance scalings in § 3 have direct implications for what curvature information is resolvable under finite evaluation complexity at initialization. To illustrate this point, we report simple budget-matched optimization trajectories for global and termwise local averaged objectives.

We consider  $(n, L) = (18, 8)$  and compare stochastic gradient descent (SGD) [1] with a representative geometry-aware first-order method, the quantum natural gradient (QNG) [33], using matched iteration complexity and fixed step-size schedules. QNG is included only as a preconditioned first-order baseline; the purpose is not an optimizer comparison but an illustration of budget-limited signal resolution near initialization.

Fig. 8 shows mean cost trajectories with one-standard-deviation bands over random initializations. For the global objective  $C_{\text{global}}$  (red), both SGD and QNG exhibit negligible progress at the displayed resolution, and trajectories concentrate tightly across seeds. In contrast, the termwise averaged local objective  $C_{\text{local}}$  (blue) decreases reliably and shows appreciable seed-to-seed variability under the same budget. These

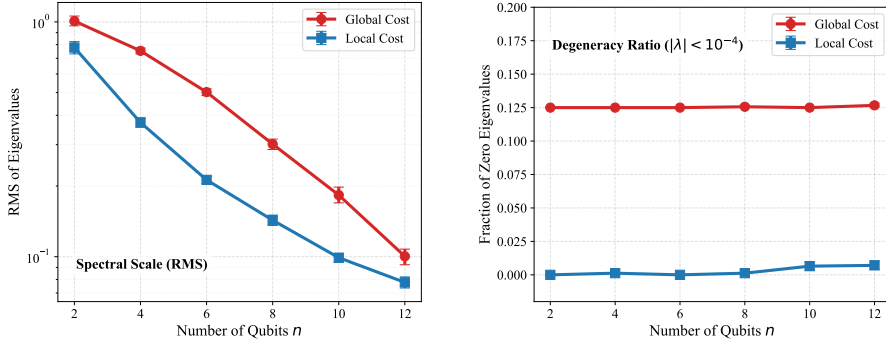


Fig. 7: **Quantitative diagnostics of the Hessian spectrum at initialization.** (Left) RMS eigenvalue versus  $n$  for the global cost (red circles) and local averaged cost (blue squares). (Right) Thresholded near-zero eigenvalue fraction with  $\varepsilon = 10^{-4}$ .

observations are consistent with the entrywise variance regimes in § 3 and with the finite-budget interpretation of Corollary 3.8: under a fixed estimator resolution, global objectives quickly lose resolvable descent directions at initialization, whereas locality preserves observable signals over the same depth and budget.

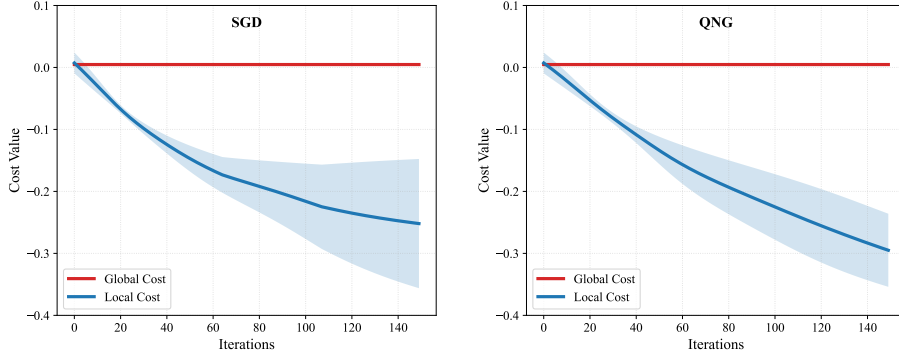


Fig. 8: **Budget-limited optimization trajectories at  $(n, L) = (18, 8)$ .** Mean cost versus iteration for  $C_{\text{global}}$  (red) and  $C_{\text{local}}$  (blue): SGD (left) and QNG (right). Shading:  $\pm 1$  standard deviation over random initializations.

**5. Conclusion.** In this study, we have systematically analyzed the second-order trainability of variational quantum algorithms by quantifying the initialization scaling of Hessian-entry fluctuations. By leveraging exact parameter-shift rules to map entrywise variances to finite covariance quadratic forms, we established a fundamental dichotomy in the statistical resolvability of curvature information. For global objectives, the Hessian inherits exponential concentration, implying that resolving curvature requires a prohibitive exponential sampling budget. Conversely, for termwise  $k$ -local objectives, the variance decay is polynomial and governed by the causal lightcone volume. These findings delineate the precise boundary where second-order information

remains computationally accessible, a distinction that is rigorously supported by our numerical experiments across varying system configurations.

Several avenues remain for future research. Theoretically, identifying conditions under which entrywise resolvability implies favorable matrix conditioning would strengthen the link to optimizer convergence. Practically, extending this variance-based framework to realistic noise models is essential for NISQ applications. Broadening the scope, our findings on derivative scaling have direct implications for advanced computational paradigms that rely on higher-order information, including quantum multiscale modeling [12, 14, 8] and quantum machine learning [15, 23]. Understanding the resolvability limits in these contexts will be crucial for developing robust quantum algorithms for complex scientific computing tasks.

## Appendix A. Proofs.

### A.1. Covariance–quadratic representations from parameter shifts.

#### A.1.1. Proof of Lemma 2.6.

*Proof.* All expectations, variances, and covariances are with respect to the initialization  $\boldsymbol{\theta} \sim \rho$ . Under Assumption 2.4,  $|C(\boldsymbol{\theta})| \leq \|O\| \leq 1$ , so all second moments exist. By the diagonal second-order parameter-shift identity (2.12), define

$$C_+ := C(\boldsymbol{\theta} + \pi \mathbf{e}_j), \quad C_0 := C(\boldsymbol{\theta}), \quad C_- := C(\boldsymbol{\theta} - \pi \mathbf{e}_j).$$

Then

$$H_{jj} = \frac{1}{4}(C_+ - 2C_0 + C_-) = \sum_{\alpha \in \{+, 0, -\}} a_\alpha C_\alpha, \quad (a_+, a_0, a_-) = \frac{1}{4}(1, -2, 1).$$

Using  $\text{Var}(\sum_\alpha a_\alpha C_\alpha) = \sum_{\alpha, \beta} a_\alpha a_\beta \text{Cov}(C_\alpha, C_\beta)$  yields

$$\text{Var}(H_{jj}) = \sum_{\alpha, \beta \in \{+, 0, -\}} a_\alpha a_\beta \text{Cov}(C_\alpha, C_\beta) = a^\top \Sigma a,$$

where  $\Sigma_{\alpha\beta} := \text{Cov}(C_\alpha, C_\beta)$ . This proves (2.13). Expanding the quadratic form gives

$$\begin{aligned} \text{Var}(H_{jj}) &= \frac{1}{16} \left( \text{Var}(C_+) + \text{Var}(C_-) + 4 \text{Var}(C_0) + 2 \text{Cov}(C_+, C_-) \right. \\ &\quad \left. - 4 \text{Cov}(C_+, C_0) - 4 \text{Cov}(C_-, C_0) \right). \end{aligned}$$

which is an explicit linear combination of variances and covariances among  $\{C_+, C_0, C_-\}$ .  $\blacksquare$  as stated in Lemma 2.6.  $\square$

#### A.1.2. Off-diagonal entries.

LEMMA A.1 (Covariance–quadratic form for off-diagonal Hessian entries). *Let  $j \neq k$  and define the four shifted costs*

$$C_{\sigma\tau} := C\left(\boldsymbol{\theta} + \sigma \frac{\pi}{2} \mathbf{e}_j + \tau \frac{\pi}{2} \mathbf{e}_k\right), \quad \sigma, \tau \in \{+, -\}.$$

*Then (2.8) implies*

$$H_{jk} = \frac{1}{4}(C_{++} - C_{+-} - C_{-+} + C_{--}).$$

Let  $c := (C_{++}, C_{+-}, C_{-+}, C_{--})^\top$  and  $s := (1, -1, -1, 1)^\top$ , and set  $\Sigma := \text{Cov}(c) \in \mathbb{R}^{4 \times 4}$ . Then we have  $\text{Var}(H_{jk}) = \frac{1}{16} s^\top \Sigma s$ . Equivalently,

$$(A.1) \quad \text{Var}(H_{jk}) = \frac{1}{16} \sum_{\sigma, \tau \in \{+, -\}} \sum_{\sigma', \tau' \in \{+, -\}} s_{\sigma\tau} s_{\sigma'\tau'} \text{Cov}(C_{\sigma\tau}, C_{\sigma'\tau'}),$$

where  $s_{++} = s_{--} = 1$  and  $s_{+-} = s_{-+} = -1$ .

*Proof.* The mixed second-order parameter-shift identity (2.8) gives the stated linear combination of the four shifted costs. For any random vector  $c$  and deterministic  $a$ ,  $\text{Var}(a^\top c) = a^\top \text{Cov}(c) a$ . Applying this with  $a = \frac{1}{4}s$  and expanding the quadratic form gives (A.1).  $\square$

*Remark A.2.* More generally, any differentiation scheme that represents a derivative quantity as a finite linear combination of shifted costs,

$$X(\boldsymbol{\theta}) = \sum_{\ell=1}^m a_\ell C(\boldsymbol{\theta} \oplus s_\ell), \quad m < \infty,$$

admits the covariance–quadratic representation

$$\text{Var}_\rho(X) = \sum_{\ell, \ell'=1}^m a_\ell a_{\ell'} \text{Cov}_\rho(C(\boldsymbol{\theta} \oplus s_\ell), C(\boldsymbol{\theta} \oplus s_{\ell'})).$$

In our setting, the relevant shift sets have constant size  $m = O(1)$  determined only by the chosen parameter-shift rule.

**A.2. Covariance bounds under bounded spreading.** For an observable  $O$ , define its Heisenberg evolution under the circuit by  $O(\boldsymbol{\theta}) := U^\dagger(\boldsymbol{\theta}) O U(\boldsymbol{\theta})$ . Under Assumptions 2.1–2.3, there exists a backward-lightcone radius  $R_L = O(rL)$  such that conjugation expands the support of any  $k$ -local operator to at most an  $R_L$ -neighborhood on the interaction graph  $G$ .

LEMMA A.3 (Finite-range independence and a uniform covariance bound). *Under Assumptions 2.1, 2.3, and 2.4, and under the initialization model in § 2.4, let  $A$  and  $B$  be Hermitian operators with  $\|A\| \leq 1$  and  $\|B\| \leq 1$ . Let  $\Lambda_A := \text{supp}(A)$  and  $\Lambda_B := \text{supp}(B)$ , and define the random variables*

$$X(\boldsymbol{\theta}) := \langle 0 | A(\boldsymbol{\theta}) | 0 \rangle, \quad Y(\boldsymbol{\theta}) := \langle 0 | B(\boldsymbol{\theta}) | 0 \rangle,$$

where  $A(\boldsymbol{\theta}) = U(\boldsymbol{\theta})^\dagger A U(\boldsymbol{\theta})$  and  $B(\boldsymbol{\theta}) = U(\boldsymbol{\theta})^\dagger B U(\boldsymbol{\theta})$ . Let  $d := \text{dist}_G(\Lambda_A, \Lambda_B)$  be the graph distance between the supports. Then:

(i) *If  $d > 2R_L$ , then  $X(\boldsymbol{\theta})$  and  $Y(\boldsymbol{\theta})$  are independent and hence*

$$(A.2) \quad \text{Cov}_\rho(X, Y) = 0.$$

(ii) *For all  $d$ , one has*

$$(A.3) \quad |\text{Cov}_\rho(X, Y)| \leq 1.$$

*Consequently,*

$$(A.4) \quad |\text{Cov}_\rho(X, Y)| \leq \mathbf{1}\{d \leq 2R_L\}.$$

*Remark A.4.* Lemma A.3 uses only bounded operator spreading and independence of initialization parameters. It yields a hard-cutoff correlation structure: beyond distance  $2R_L$  the covariance vanishes, while for  $d \leq 2R_L$  we only use the trivial bound  $|\text{Cov}_\rho(X, Y)| \leq 1$ . No nontrivial decay inside the lightcone is claimed.

*Proof.* By Assumptions 2.1–2.3,  $A(\boldsymbol{\theta})$  is supported within the  $R_L$ -neighborhood of  $\Lambda_A$  and  $B(\boldsymbol{\theta})$  is supported within the  $R_L$ -neighborhood of  $\Lambda_B$ . Equivalently,  $X(\boldsymbol{\theta})$  depends only on the subset of parameters associated with gates whose qubit supports intersect the backward lightcone of  $\Lambda_A$ , and likewise  $Y(\boldsymbol{\theta})$  depends only on parameters within the backward lightcone of  $\Lambda_B$ .

If  $d > 2R_L$ , these two backward lightcones are disjoint, hence the corresponding parameter subsets are disjoint. Under the initialization model in § 2.4, parameters on disjoint subsets are independent, so  $X(\boldsymbol{\theta})$  and  $Y(\boldsymbol{\theta})$  are independent, proving (A.2).

For (A.3), unitary conjugation preserves operator norm, so  $\|A(\boldsymbol{\theta})\| = \|A\| \leq 1$  and  $\|B(\boldsymbol{\theta})\| = \|B\| \leq 1$ . Therefore  $|X(\boldsymbol{\theta})| \leq 1$  and  $|Y(\boldsymbol{\theta})| \leq 1$ , implying  $\text{Var}_\rho(X) \leq 1$  and  $\text{Var}_\rho(Y) \leq 1$ . Cauchy–Schwarz gives  $|\text{Cov}_\rho(X, Y)| \leq \sqrt{\text{Var}_\rho(X)} \sqrt{\text{Var}_\rho(Y)} \leq 1$ , proving (A.3). Finally, (A.4) is the immediate combination of (i) and (ii).  $\square$

### A.3. A dependency-graph variance bound.

LEMMA A.5 (Variance bound via a dependency graph). *Let  $\{X_i\}_{i=1}^n$  be real-valued random variables with finite second moments, and let  $G_{\text{dep}} = (\{1, \dots, n\}, E)$  be a dependency graph in the following sense: for any disjoint index sets  $I, J \subseteq \{1, \dots, n\}$  with no edges between  $I$  and  $J$ , the families  $\{X_i\}_{i \in I}$  and  $\{X_j\}_{j \in J}$  are independent. Let  $\Delta_{\text{dep}}$  be the maximum degree of  $G_{\text{dep}}$ . Then*

$$(A.5) \quad \text{Var}\left(\sum_{i=1}^n X_i\right) \leq (\Delta_{\text{dep}} + 1) \sum_{i=1}^n \text{Var}(X_i).$$

Consequently, for  $Z := \frac{1}{n} \sum_{i=1}^n X_i$ ,

$$(A.6) \quad \text{Var}(Z) \leq \frac{\Delta_{\text{dep}} + 1}{n^2} \sum_{i=1}^n \text{Var}(X_i).$$

*Proof.* Expand the variance:

$$\text{Var}\left(\sum_{i=1}^n X_i\right) = \sum_{i=1}^n \text{Var}(X_i) + 2 \sum_{1 \leq i < j \leq n} \text{Cov}(X_i, X_j).$$

If  $\{i, j\} \notin E$ , then there is no edge between  $\{i\}$  and  $\{j\}$ , hence  $X_i$  and  $X_j$  are independent by the dependency-graph property, so  $\text{Cov}(X_i, X_j) = 0$ . Therefore,

$$\text{Var}\left(\sum_{i=1}^n X_i\right) = \sum_{i=1}^n \text{Var}(X_i) + 2 \sum_{\{i, j\} \in E, i < j} \text{Cov}(X_i, X_j).$$

Taking absolute values and applying Cauchy–Schwarz gives

$$|\text{Cov}(X_i, X_j)| \leq \sqrt{\text{Var}(X_i) \text{Var}(X_j)} \leq \frac{1}{2} (\text{Var}(X_i) + \text{Var}(X_j)).$$

Hence,

$$\begin{aligned} \text{Var}\left(\sum_{i=1}^n X_i\right) &\leq \sum_{i=1}^n \text{Var}(X_i) + 2 \sum_{\{i,j\} \in E, i < j} \frac{1}{2} (\text{Var}(X_i) + \text{Var}(X_j)) \\ &= \sum_{i=1}^n \text{Var}(X_i) + \sum_{\{i,j\} \in E} (\text{Var}(X_i) + \text{Var}(X_j)). \end{aligned}$$

Each  $\text{Var}(X_i)$  appears in the edge-sum exactly  $\deg(i)$  times, hence

$$\sum_{\{i,j\} \in E} (\text{Var}(X_i) + \text{Var}(X_j)) = \sum_{i=1}^n \deg(i) \text{Var}(X_i) \leq \Delta_{\text{dep}} \sum_{i=1}^n \text{Var}(X_i).$$

Combining these yields (A.5), and (A.6) follows by dividing by  $n^2$ .  $\square$

#### A.4. Proof of Theorem 3.3.

*Proof.* All expectations, variances, and covariances are with respect to the initialization law  $\boldsymbol{\theta} \sim \rho$ ; write  $\text{Var} \equiv \text{Var}_\rho$  and  $\text{Cov} \equiv \text{Cov}_\rho$ .

*Step 0: Finite-shift covariance representations.* By the parameter-shift identities (Assumption 2.1), each Hessian entry  $H_{jk}$  can be written as a finite linear combination of shifted costs:

$$H_{jk} = \sum_{s \in \mathcal{S}_{ab}} a_s C(\boldsymbol{\theta} \oplus s), \quad |\mathcal{S}_{ab}| = O(1).$$

Hence

$$(A.7) \quad \text{Var}(H_{jk}) = \sum_{s, s' \in \mathcal{S}_{ab}} a_s a_{s'} \text{Cov}(C(\boldsymbol{\theta} \oplus s), C(\boldsymbol{\theta} \oplus s')).$$

For diagonal entries one may take  $\mathcal{S}_{jj} = \{+\pi e_j, 0, -\pi e_j\}$  and recover (2.13); for off-diagonal entries one may take  $\mathcal{S}_{jk} = \{\pm \frac{\pi}{2} e_j \pm \frac{\pi}{2} e_k\}$  and recover Lemma A.1. It therefore suffices to control covariances between shifted costs.

Throughout, Assumption 2.4 implies  $|C(\cdot)| \leq 1$ , and thus  $|\text{Cov}(\cdot, \cdot)| \leq 1$ .

*Step 1: Global objectives.* Assume  $|\text{supp}(O)| = \Theta(n)$  and Assumption 3.1 holds. By shift-invariance of  $\rho$  on the torus (see Lemma B.1), for every fixed shift  $s$  in a finite shift set,

$$\text{Var}(C(\boldsymbol{\theta} \oplus s)) = \text{Var}(C(\boldsymbol{\theta})) \leq c_g(r, L) e^{-\alpha(r, L)n}.$$

Then for any  $s, s'$  in the same finite set, Cauchy–Schwarz yields

$$|\text{Cov}(C(\boldsymbol{\theta} \oplus s), C(\boldsymbol{\theta} \oplus s'))| \leq \sqrt{\text{Var}(C(\boldsymbol{\theta} \oplus s)) \text{Var}(C(\boldsymbol{\theta} \oplus s'))} \leq c_g(r, L) e^{-\alpha(r, L)n}.$$

Substituting this uniform bound into (A.7) and using that  $|\mathcal{S}_{ab}| = O(1)$  gives

$$\text{Var}(H_{jk}) \leq \tilde{c}(r, L) e^{-\tilde{\alpha}(r, L)n},$$

for constants depending only on  $(r, L)$  and the chosen shift rule (via  $\{a_s\}$  and  $|\mathcal{S}_{ab}|$ ). This proves (3.4).

*Step 2: Termwise local averaged objectives (polynomial scaling).* Assume the objective is of the termwise local averaged form

$$C(\boldsymbol{\theta}) = \frac{1}{n} \sum_{v=1}^n \langle 0 | O_v(\boldsymbol{\theta}) | 0 \rangle, \quad O_v(\boldsymbol{\theta}) := U(\boldsymbol{\theta})^\dagger O_v U(\boldsymbol{\theta}), \quad \|O_v\| \leq 1,$$

where each  $O_v$  is supported on at most  $k$  qubits (with  $k$  independent of  $n$ ). Fix any shift  $s$ . Define the local random variables

$$X_v^{(s)}(\boldsymbol{\theta}) := \langle 0 | U(\boldsymbol{\theta} \oplus s)^\dagger O_v U(\boldsymbol{\theta} \oplus s) | 0 \rangle, \quad C(\boldsymbol{\theta} \oplus s) = \frac{1}{n} \sum_{v=1}^n X_v^{(s)}(\boldsymbol{\theta}).$$

Shifting parameters does not change the circuit geometry, hence the backward-lightcone radius remains  $O(rL)$  for every  $s$ . By bounded spreading (Assumptions 2.1–2.3),  $X_v^{(s)}$  depends only on parameters in the backward lightcone of  $\text{supp}(O_v)$ , whose qubit support is contained in a  $(k+rL)$ -neighborhood. Therefore, if  $\text{dist}_G(\text{supp}(O_v), \text{supp}(O_w)) > k + 2rL$ , the parameter sets influencing  $X_v^{(s)}$  and  $X_w^{(s')}$  are disjoint, and the two variables are independent (Lemma A.3).

Construct a dependency graph on vertices  $\{1, \dots, n\}$  by connecting  $v \sim w$  whenever  $\text{dist}_G(\text{supp}(O_v), \text{supp}(O_w)) \leq k + 2rL$ . Its maximum degree is bounded by  $\Delta_{\text{dep}} \leq V_G(k + 2rL) - 1$ . Since  $|X_v^{(s)}| \leq 1$ , we have  $\text{Var}(X_v^{(s)}) \leq 1$ . Applying Lemma A.5 to  $\sum_v X_v^{(s)}$  yields the uniform bound (in  $s$ )

$$(A.8) \quad \text{Var}(C(\boldsymbol{\theta} \oplus s)) = \text{Var}\left(\frac{1}{n} \sum_{v=1}^n X_v^{(s)}\right) \leq \frac{\Delta_{\text{dep}} + 1}{n^2} \sum_{v=1}^n \text{Var}(X_v^{(s)}) \leq \frac{V_G(k + 2rL)}{n}.$$

The same construction applies to cross-covariances between two shifts  $s$  and  $s'$ : independence still holds whenever  $\text{dist}_G(\text{supp}(O_v), \text{supp}(O_w)) > k + 2rL$ , so the same dependency-graph argument gives

$$(A.9) \quad |\text{Cov}(C(\boldsymbol{\theta} \oplus s), C(\boldsymbol{\theta} \oplus s'))| \leq \frac{V_G(k + 2rL)}{n}, \quad \forall s, s' \text{ in a fixed finite shift set.}$$

Finally, substitute (A.9) into the covariance–quadratic representation (A.7). Since  $|\mathcal{S}_{ab}| = O(1)$  and the coefficients  $\{a_s\}$  are constants determined by the shift rule, we obtain

$$\text{Var}(H_{jk}) \leq c_{\text{loc}}(k, r, L) \frac{V_G(k + 2rL)}{n},$$

for some constant  $c_{\text{loc}}(k, r, L) > 0$ . This proves (3.5). The lattice-growth specialization (3.6) follows immediately from  $V_G(m) = O(m^D)$ .  $\square$

## Appendix B. Supplementary.

### B.1. Uniformity over finite shift sets.

LEMMA B.1 (Uniform concentration over finite shift sets). *Let  $\mathcal{S} \subset \mathbb{R}^M$  be any finite set of shifts and interpret parameters on the torus  $\mathbb{T}^M = (\mathbb{R}/2\pi\mathbb{Z})^M$ . Suppose the initialization distribution  $\rho$  on  $\mathbb{T}^M$  is shift-invariant with respect to  $\mathcal{S}$ , i.e.,*

$$(B.1) \quad \boldsymbol{\theta} \sim \rho \implies \boldsymbol{\theta} \oplus s \sim \rho, \quad \forall s \in \mathcal{S},$$

where  $\oplus$  denotes addition modulo  $2\pi$  componentwise. Then Assumption 3.1 implies

$$(B.2) \quad \sup_{s \in \mathcal{S}} \text{Var}_\rho [C(\boldsymbol{\theta} \oplus s)] \leq c_g(r, L) e^{-\alpha(r, L)n}.$$

*Proof.* Fix  $s \in \mathcal{S}$ . By (B.1), the random variables  $C(\boldsymbol{\theta})$  and  $C(\boldsymbol{\theta} \oplus s)$  have the same distribution under  $\rho$ , hence  $\text{Var}_\rho[C(\boldsymbol{\theta} \oplus s)] = \text{Var}_\rho[C(\boldsymbol{\theta})]$ . Taking the supremum over  $s \in \mathcal{S}$  yields (B.2).  $\square$

If  $\rho$  is the product of i.i.d. uniform measures on  $[0, 2\pi)$ , then (B.1) holds for any finite shift set  $\mathcal{S}$  arising in parameter-shift rules.

## B.2. A sufficient design-based route for global concentration.

*How to verify Assumption 3.1.* Assumption 3.1 can be supported (i) theoretically via design/mixing conditions, and/or (ii) empirically by Monte Carlo sampling  $\boldsymbol{\theta}^{(m)} \sim \rho$  and estimating  $\text{Var}_\rho[C(\boldsymbol{\theta})]$  from the sample variance. By Lemma B.1, the same empirical test applies uniformly over the finite shift set used in parameter-shift rules.

**PROPOSITION B.2** (A sufficient condition for Assumption 3.1). *Let  $d = 2^n$ . Assume the induced state ensemble  $\{|\psi(\boldsymbol{\theta})\rangle := U(\boldsymbol{\theta})|0\rangle\}_{\boldsymbol{\theta} \sim \rho}$  forms an exact complex projective 2-design on  $\mathbb{C}^d$ . Then for any Hermitian observable  $O$ ,*

$$(B.3) \quad \text{Var}_\rho[\langle\psi(\boldsymbol{\theta})|O|\psi(\boldsymbol{\theta})\rangle] = \frac{\text{Tr}(O^2) - \text{Tr}(O)^2/d}{d(d+1)}.$$

In particular, if  $\|O\| \leq 1$  then  $\text{Tr}(O^2) \leq d$ , hence

$$(B.4) \quad \text{Var}_\rho[C(\boldsymbol{\theta})] \leq \frac{1}{d+1} = \mathcal{O}(2^{-n}),$$

so Assumption 3.1 holds with  $\alpha = \log 2$  up to constants.

*Proof.* Let  $|\psi\rangle$  be distributed according to an exact projective 2-design on  $\mathbb{C}^d$ . By the defining second-moment property of a projective 2-design, the second moment operator matches Haar:

$$(B.5) \quad \mathbb{E}[|\psi\rangle\langle\psi|^{\otimes 2}] = \frac{I+F}{d(d+1)},$$

where  $F$  is the swap operator on  $\mathbb{C}^d \otimes \mathbb{C}^d$ . Then

$$\mathbb{E}[\langle\psi|O|\psi\rangle] = \text{Tr}\left(O\mathbb{E}[|\psi\rangle\langle\psi|]\right) = \frac{\text{Tr}(O)}{d},$$

using  $\mathbb{E}[|\psi\rangle\langle\psi|] = I/d$ . For the second moment, use the swap trick:

$$\langle\psi|O|\psi\rangle^2 = \text{Tr}((O \otimes O)|\psi\rangle\langle\psi|^{\otimes 2}),$$

hence by (B.5),

$$\mathbb{E}[\langle\psi|O|\psi\rangle^2] = \text{Tr}\left((O \otimes O)\frac{I+F}{d(d+1)}\right) = \frac{\text{Tr}(O)^2 + \text{Tr}(O^2)}{d(d+1)}.$$

Subtracting the squared mean  $(\text{Tr}(O)/d)^2$  yields (B.3). If  $\|O\| \leq 1$ , then  $\text{Tr}(O^2) \leq d\|O\|^2 \leq d$ , giving (B.4).  $\square$

We do not claim that modest-depth hardware-efficient ansätze form 2-designs; the proposition is included only as a verifiable sufficient route to global concentration when design/mixing guarantees are available.

**B.3. From entry-wise second moments to matrix norm bounds.** We state in Lemma 3.6 the corresponding matrix norm implications in the main text; we provide a complete proof here for completeness.

LEMMA B.3 (From entry-wise second moments to Frobenius and spectral norm bounds). *Let  $H \in \mathbb{R}^{M \times M}$  be a random matrix with finite second moments. Then*

$$(B.6) \quad \mathbb{E}\|H\|_F^2 = \sum_{j,k=1}^M \mathbb{E}[H_{jk}^2] = \sum_{j,k=1}^M \left( \text{Var}(H_{jk}) + (\mathbb{E}[H_{jk}])^2 \right).$$

Moreover, since  $\|H\|_2 \leq \|H\|_F$  pointwise, we have the second-moment bound

$$(B.7) \quad \mathbb{E}\|H\|_2^2 \leq \mathbb{E}\|H\|_F^2,$$

and by Jensen's inequality,

$$(B.8) \quad \mathbb{E}\|H\|_2 \leq \mathbb{E}\|H\|_F \leq \sqrt{\mathbb{E}\|H\|_F^2}.$$

In particular, if  $\text{Var}(H_{jk}) \leq v_n$  for all  $j, k$  and  $|\mathbb{E}H_{jk}| \leq \mu_n$  for all  $j, k$ , then

$$(B.9) \quad \mathbb{E}\|H\|_F^2 \leq M^2(v_n + \mu_n^2), \quad \mathbb{E}\|H\|_2^2 \leq M^2(v_n + \mu_n^2), \quad \mathbb{E}\|H\|_2 \leq M\sqrt{v_n + \mu_n^2}.$$

COROLLARY B.4 (Curvature magnitude scale (entry-wise to global norms)). *Under the hypotheses of Theorem 3.3, suppose additionally that there exists a constant  $c > 0$  independent of  $n$  such that for all  $j, k$ ,*

$$|\mathbb{E}[H_{jk}]| \leq \mu_n \quad \text{and} \quad \mu_n^2 \leq c v_n,$$

where  $v_n$  denotes the entry-wise variance bound from Theorem 3.3. Then

$$\mathbb{E}\|H\|_F^2 \lesssim M^2 v_n, \quad \mathbb{E}\|H\|_2^2 \lesssim M^2 v_n, \quad \mathbb{E}\|H\|_2 \lesssim M\sqrt{v_n}.$$

These bounds quantify a global magnitude scale for curvature at initialization (and hence for the typical size of Hessian–vector products), but they do not, by themselves, determine conditioning,  $\lambda_{\min}(H)$ , or near-singularity without further spectral information.

## REFERENCES

- [1] S.-I. AMARI, *Backpropagation and stochastic gradient descent method*, Neurocomputing, 5 (1993), pp. 185–196.
- [2] D. AN, J.-P. LIU, AND L. LIN, *Linear combination of hamiltonian simulation for nonunitary dynamics with optimal state preparation cost*, Physical Review Letters, 131 (2023), p. 150603.
- [3] A. ARRASMITH ET AL., *Equivalence of quantum barren plateaus to cost concentration and narrow gorges*, Quantum Sci. Technol., 7 (2022), p. 045015, <https://doi.org/10.1088/2058-9565/ac7d06>.
- [4] V. BERGHELM, J. IZAAC, M. SCHULD, C. GOGOLIN, S. AHMED, V. AJITH, M. S. ALAM, G. ALONSO-LINAJE, B. AKASHNARAYANAN, A. ASADI, ET AL., *Pennylane: Automatic differentiation of hybrid quantum-classical computations*, arXiv preprint arXiv:1811.04968, (2018).
- [5] K. BHARTI, A. CERVERA-LIERTA, T. H. KYAW, T. HAUG, S. ALPERIN-LEA, A. ANAND, M. DEGROOTE, H. HEIMONEN, J. S. KOTTMANN, T. MENKE, W. K. MOK, S. SIM, L.-C. KWEK, AND A. ASPURU-GUZIK, *Noisy intermediate-scale quantum (nisq) algorithms*, Reviews of Modern Physics, 94 (2022), p. 015004, <https://doi.org/10.1103/RevModPhys.94.015004>.

- [6] L. BITTEL AND M. KLIESCH, *Training variational quantum algorithms is np-hard*, Phys. Rev. Lett., 127 (2021), p. 120502, <https://doi.org/10.1103/PhysRevLett.127.120502>, <https://link.aps.org/doi/10.1103/PhysRevLett.127.120502>.
- [7] J. BOWLES, D. WIERICH, AND C.-Y. PARK, *Backpropagation scaling in parameterised quantum circuits*, Quantum, 9 (2025), p. 1873, <https://doi.org/10.22331/q-2025-10-02-1873>, <https://arxiv.org/abs/2306.14962>.
- [8] J. BRAUN, C. ORTNER, Y. WANG, AND L. ZHANG, *Higher-order far-field boundary conditions for crystalline defects*, SIAM Journal on Numerical Analysis, 63 (2025), pp. 520–541.
- [9] M. CEREZO, A. ARRAS, R. BABBUSH, S. C. BENJAMIN, S. ENDO, K. FUJII, J. R. MCCLEAN, K. MITARAI, X. YUAN, L. CINCIO, AND P. J. COLES, *Variational quantum algorithms*, Nature Reviews Physics, 3 (2021), pp. 625–644, <https://doi.org/10.1038/s42254-021-00348-9>.
- [10] M. CEREZO AND P. J. COLES, *Higher order derivatives of quantum neural networks with barren plateaus*, Quantum Sci. Technol., 6 (2021), p. 035006, <https://doi.org/10.1088/2058-9565/abf51a>.
- [11] M. CEREZO, A. SONE, T. VOLKOFF, ET AL., *Cost function dependent barren plateaus in shallow parametrized quantum circuits*, Nat Commun, 12 (2021), p. 1791, <https://doi.org/10.1038/s41467-021-21728-w>.
- [12] H. CHEN, C. ORTNER, AND Y. WANG, *Qm/mm methods for crystalline defects. part 3: Machine-learned mm models*, Multiscale Modeling & Simulation, 20 (2022), pp. 1490–1518.
- [13] G. E. CROOKS, *Gradients of parameterized quantum gates using the parameter-shift rule and gate decomposition*, arXiv preprint arXiv:1905.13311, (2019).
- [14] M. DEIML AND D. PETERSEIM, *Quantum realization of the finite element method*, Mathematics of Computation, (2025).
- [15] E. FEBRIANTO, Y. WANG, B. LIU, M. ORTIZ, AND F. CIRAK, *A quantum spectral method for non-periodic boundary value problems*, arXiv preprint arXiv:2511.11494, (2025).
- [16] E. GRANT, L. WOSSNIG, M. OSTASZEWSKI, AND M. BENEDETTI, *An initialization strategy for addressing barren plateaus in parametrized quantum circuits*, Quantum, 3 (2019), p. 214, <https://doi.org/10.22331/q-2019-12-09-214>, <https://doi.org/10.22331/q-2019-12-09-214>.
- [17] Z. HOLMES, K. SHARMA, M. CEREZO, AND P. J. COLES, *Connecting ansatz expressibility to gradient magnitudes and barren plateaus*, Physical Review Letters, 126 (2021), p. 190501, <https://doi.org/10.1103/PhysRevLett.126.190501>.
- [18] J. HU, S. JIN, N. LIU, AND L. ZHANG, *Quantum circuits for partial differential equations via schrödingerisation*, Quantum, 8 (2024), p. 1563.
- [19] S. JIN, N. LIU, AND Y. YU, *Quantum simulation of partial differential equations via schrödingerization*, Physical Review Letters, 133 (2024), p. 230602.
- [20] A. KANDALA, A. MEZZACAPPA, K. TEMME, M. TAKITA, M. BRINK, J. M. CHOW, AND J. M. GAMBETTA, *Hardware-efficient variational quantum eigensolver for small molecules and quantum magnets*, nature, 549 (2017), pp. 242–246.
- [21] M. LAROCCA, P. CZARNIK, K. SHARMA, G. MURALEEDHARAN, P. J. COLES, AND M. CEREZO, *Diagnosing barren plateaus with tools from quantum optimal control*, Quantum, 6 (2022), p. 824, <https://doi.org/10.22331/q-2022-09-29-824>, <https://arxiv.org/abs/2105.14377>.
- [22] M. LAROCCA, S. THANASILP, S. WANG, K. SHARMA, J. BIAMONTE, P. J. COLES, L. CINCIO, J. R. MCCLEAN, Z. HOLMES, AND M. CEREZO, *Barren plateaus in variational quantum computing*, Nature Reviews Physics, (2025), pp. 1–16.
- [23] X. LIU, Y. WANG, AND T. ZHAO, *Beyond adam: Disentangling optimizer effects in the fine-tuning of atomistic foundation models*, arXiv preprint arXiv:2512.05489, (2025).
- [24] C. O. MARRERO, M. KIEFEROVÁ, AND N. WIEBE, *Entanglement induced barren plateaus*, PRX Quantum, 2 (2021), p. 040316, <https://doi.org/10.1103/PRXQuantum.2.040316>.
- [25] J. R. MCCLEAN, S. BOIXO, V. N. SMELYANSKIY, R. BABBUSH, AND H. NEVEN, *Barren plateaus in quantum neural network training landscapes*, Nature Communications, 9 (2018), p. 4812, <https://doi.org/10.1038/s41467-018-07090-4>.
- [26] Q. MENG AND Y. WANG, *Trainability-oriented hybrid quantum regression via geometric preconditioning and curriculum optimization*, arXiv preprint arXiv:2601.11942, (2026).
- [27] N. A. NEMKOV, E. O. KIKTENKO, AND A. K. FEDOROV, *Barren plateaus swamped with traps*, Phys. Rev. A, 111 (2025), p. 012441, <https://doi.org/10.1103/PhysRevA.111.012441>, <https://link.aps.org/doi/10.1103/PhysRevA.111.012441>.
- [28] A. PERUZZO, J. McCLEAN, P. SHADBOLT, M. H. YUNG, X. Q. ZHOU, P. J. LOVE, A. ASPURU-GUZIK, AND J. L. O'BRIEN, *A variational eigenvalue solver on a photonic quantum processor*, Nature Communications, 5 (2014), p. 4213, <https://doi.org/10.1038/ncomms5213>, <https://doi.org/10.1038/ncomms5213>.
- [29] A. PESAH, M. CEREZO, S. WANG, T. VOLKOFF, A. T. SORNBORGER, AND P. J. COLES, *Absence of barren plateaus in quantum convolutional neural networks*, Phys. Rev. X, 11

(2021), p. 041011, <https://doi.org/10.1103/PhysRevX.11.041011>, <https://link.aps.org/doi/10.1103/PhysRevX.11.041011>.

[30] P. PFEUTY, *The one-dimensional ising model with a transverse field*, ANNALS of Physics, 57 (1970), pp. 79–90.

[31] P. SEN, A. S. BHATIA, K. S. BHANGU, AND A. ELBELTAGI, *Variational quantum classifiers through the lens of the hessian*, PLOS ONE, (2022), <https://doi.org/10.1371/journal.pone.0262346>.

[32] A. SKOLIK, J. R. MCCLEAN, M. MOHSENI, P. VAN DER SMAGT, AND M. LEIB, *Layerwise learning for quantum neural networks*, Quantum Machine Intelligence, 3 (2021), p. 5, <https://doi.org/10.1007/s42484-020-00036-4>, <https://doi.org/10.1007/s42484-020-00036-4>.

[33] J. STOKES, J. IZAAC, N. KILLORAN, AND G. CARLEO, *Quantum natural gradient*, Quantum, 4 (2020), p. 269.

[34] A. V. UVAROV AND J. D. BIAMONTE, *On barren plateaus and cost function locality in variational quantum algorithms*, J. Phys. A: Math. Theor., 54 (2021), p. 245301, <https://doi.org/10.1088/1751-8121/abfac7>.

[35] S. WANG, E. FONTANA, M. CEREZO, K. SHARMA, A. SONE, L. CINCIO, AND P. J. COLES, *Noise-induced barren plateaus in variational quantum algorithms*, Nature Communications, 12 (2021), p. 6961, <https://doi.org/10.1038/s41467-021-27045-6>.

[36] D. WIERICH, J. IZAAC, C. WANG, AND C. Y.-Y. LIN, *General parameter-shift rules for quantum gradients*, Quantum, 6 (2022), p. 677.

[37] G. ZHU, J. BIERMAN, J. LU, AND Y. LI, *Quantum circuit for non-unitary linear transformation of basis sets*, npj Quantum Information, (2025).